Supporting Information

Integrated Plasmonic Metasurfaces for Spectropolarimetry

Wei Ting Chen[1], Peter Török[2,*], Matthew R. Foreman[3], Chun Yen Liao[1],

Wei-Yi Tsai[1], Pei Ru Wu[1], and Din Ping Tsai[1,4,*]

[1]Department of Physics, National Taiwan University, Taipei 10617, Taiwan

[2]Blackett Laboratory, Department of Physics, Imperial College London, London, SW7 2BW, UK

[3]Max Planck Institute for the Science of Light, Günther-Scharowsky-Straße 1, 91058 Erlangen, Germany

[4]Research Center for Applied Sciences, Academia Sinica, Taipei 11529, Taiwan

*Corresponding authors: peter.torok@imperial.ac.uk , dptsai@phys.ntu.edu.tw

Supporting Information 1 - Nanorod scattering

In the local coordinate system of the nanorod, the optical response can heuristically be described using a diagonal scattering matrix with diagonal elements T_l and T_s describing the response of each plasmonic eigenmode excited by an electric field (of unit amplitude) polarized along the long and short axis of the nanorod respectively. In general T_l and T_s are complex quantities. Subsequently, in the global coordinate system, the scattering matrix of the nanorod is

$$\begin{bmatrix} \cos(\gamma) & -\sin(\gamma) \\ \sin(\gamma) & \cos(\gamma) \end{bmatrix} \begin{bmatrix} T_l & 0 \\ 0 & T_s \end{bmatrix} \begin{bmatrix} \cos(\gamma) & \sin(\gamma) \\ -\sin(\gamma) & \cos(\gamma) \end{bmatrix} \tag{1}$$

where γ defines the orientation of the nanorod. After some algebraic manipulation Equation 1 can be written in the form

$$\frac{T_l + T_s}{2} \begin{bmatrix} 1 & 0 \\ 0 & 1 \end{bmatrix} + \frac{T_l - T_s}{2} \begin{bmatrix} \cos(2\gamma) & \sin(2\gamma) \\ \sin(2\gamma) & -\cos(2\gamma) \end{bmatrix} \tag{2}$$

whereby it is seen that the field scattered from the nanorod can be considered as comprising two components: one with the same polarization as the incident field and the other polarized as if the incident field passed through a half wave plate. Incident x-polarized and right-handed circularly polarized light accordingly gives rise to an output complex electric field described by the Jones vectors

$$\vec{E} = \frac{1}{2}\left[(T_l + T_s) \begin{pmatrix} 1 \\ 0 \end{pmatrix} + (T_l \text{-} T_s) \begin{pmatrix} \cos(2\gamma) \\ \sin(2\gamma) \end{pmatrix} \right] \tag{3}$$

and

$$\vec{E} = \frac{1}{2}\left[(T_l + T_s) \begin{pmatrix} 1 \\ -i \end{pmatrix} + (T_l - T_s) \begin{pmatrix} 1 \\ i \end{pmatrix} \exp(2i\gamma) \right] \tag{4}$$

respectively. From Equation 3 it is evident that for $\gamma = 45^\circ$ we expect a y-polarized component in the output that has a π phase difference compared to the case when $\gamma = -45^\circ$. This property has been verified experimentally in Ref. [1]. Furthermore, when the incident polarization of light is polarized along the long axis of the nanorod, i.e. $\gamma = 0^{\circ}$, the output electric field is dependent only on T_l. Control of the phase imparted on the scattered light can thus be achieved through variation of its width and length as shown in Figures S1(a)-(d). By forming an array of nanorods of different geometry a linear gradient in the phase discontinuity can be achieved as discussed in the main text. Similarly, for scattering of right circularly polarized (RCP) light we expect a left circularly polarized (LCP) component with a phase delay dependent on the nanorod orientation in addition to a background RCP contribution. Indeed, with reference to Figure S1(e)-(h) this prediction is borne out in full electromagnetic simulations (see below).

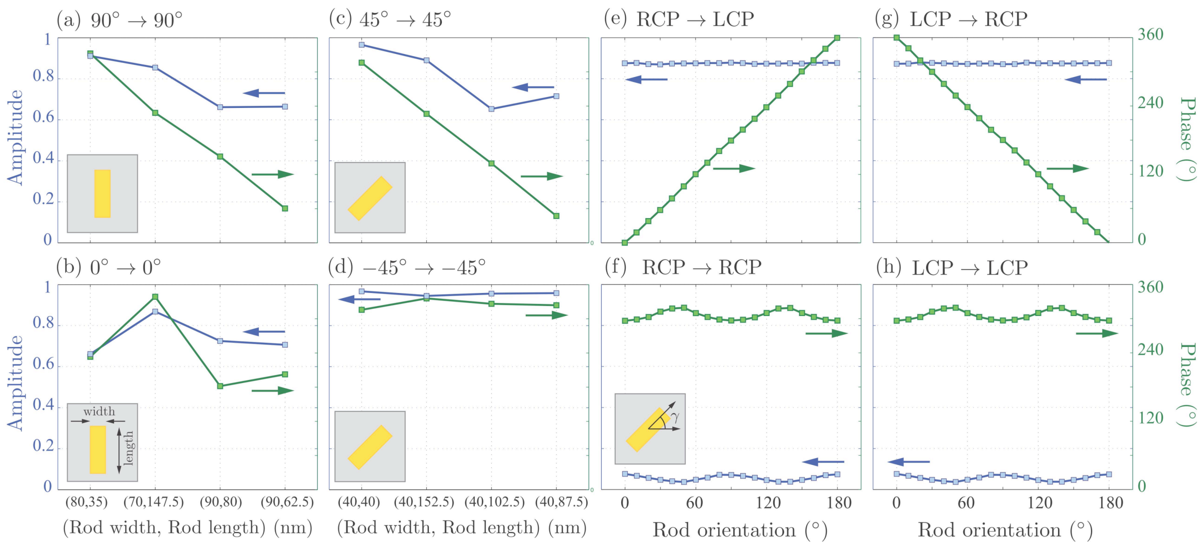

Figure S1. Simulated nanorod scattering response. (a) Amplitude and phase of vertically polarised plane wave (λ = 700 nm) diffracted from a periodic array of identical vertically aligned nanorods for different nanorod geometries. (b) As (a) but for a plane wave polarised perpendicularly to the nanorod long axis. Similarly (c) and (d) show the diffracted amplitude and phase for a nanorods oriented at 45° under $\pm 45^{\circ}$ polarised illumination. (e)-(h) show simulated amplitude and phase of LCP and RCP components of light reflected from 140 nm × 70 nm nanorods of differing orientation under circularly polarised illumination.

To further verify our heuristic model of nanorod response to incident circularly polarized light we have performed *S*-parameter based calculations, in addition to finite element calculations using COMSOL for nanorods of differing aspect ratios. Specifically we calculated the scattered amplitude of right and left circularly polarized components under a right circularly polarized illumination. Results are shown in Figure S2, as the nanorod aspect ratio decreases to 1 whereby $T_l = T_s$. As the aspect ratio decreases a weaker LCP component is expected as agrees well with the numerical calculation shown in Figure S2(b).

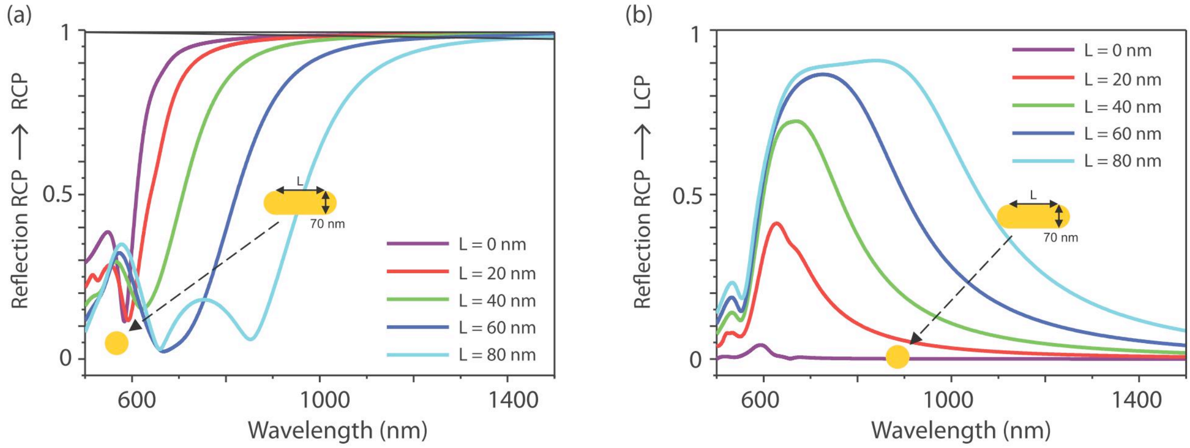

Figure S2. (a) Scattered amplitude of the right circularly polarized beam from nanorods of varying aspect ratios when illuminated by right circularly polarized light, calculated using a *S*-parameter based approach. (b) As (a) except the left circularly polarized component of the scattered wave is considered.

Supporting Information 2 - Electromagnetic simulations

Electromagnetic simulations of the phase modulation and reflectance of periodic arrays of gold nanorod structures were implemented using the commercial CST microwave studio software package. Simulation geometry comprised of 50 nm thick Au nanorods on top of a 40 nm thick SiO_2 spacer layer on a gold mirror. Periodic boundary conditions were used with *x* and *y* periods of 150 nm and 200 nm respectively. *S*-parameters, i.e. reflected phase and amplitude, were determined for a normally incident plane wave polarized at 0°, ±45°, and 90° to the horizontal. Results for incident circular polarized states were found through appropriate superposition of the linear states. Far field diffraction patterns from nanorod arrays were determined using COMSOL 3.5a. The refractive index of the SiO_2 spacer was taken as $n_{SiO2} = 1.5$. The permittivity data of bulk gold was taken from Ref. [2].

Supporting Information 3 - Extinction ratios

Although each metasurface is engineered so as to direct light of a given polarization into the collection optics, an orthogonally-polarized cross-talk component is nevertheless present. For example, in the case of the linear channels this background arises due to weak excitation of plasmon oscillations along the short axis of the nanorods. The numerically calculated extinction ratio for each polarization channel is plotted in Figures S3 and S4. In Figure S3 we show plots of the angular diffraction pattern from each metasurface based polarization analyser when illuminated normally with the nominal polarization state and for the orthogonally polarized case. In Figure S4, we compare the extinction ratio of each metasurface as a function of wavelength. Superior performance is found in the circular channels with typical extinction ratios of $\sim 400 - 2000$. Linear channels generally see better performance at longer wavelengths.

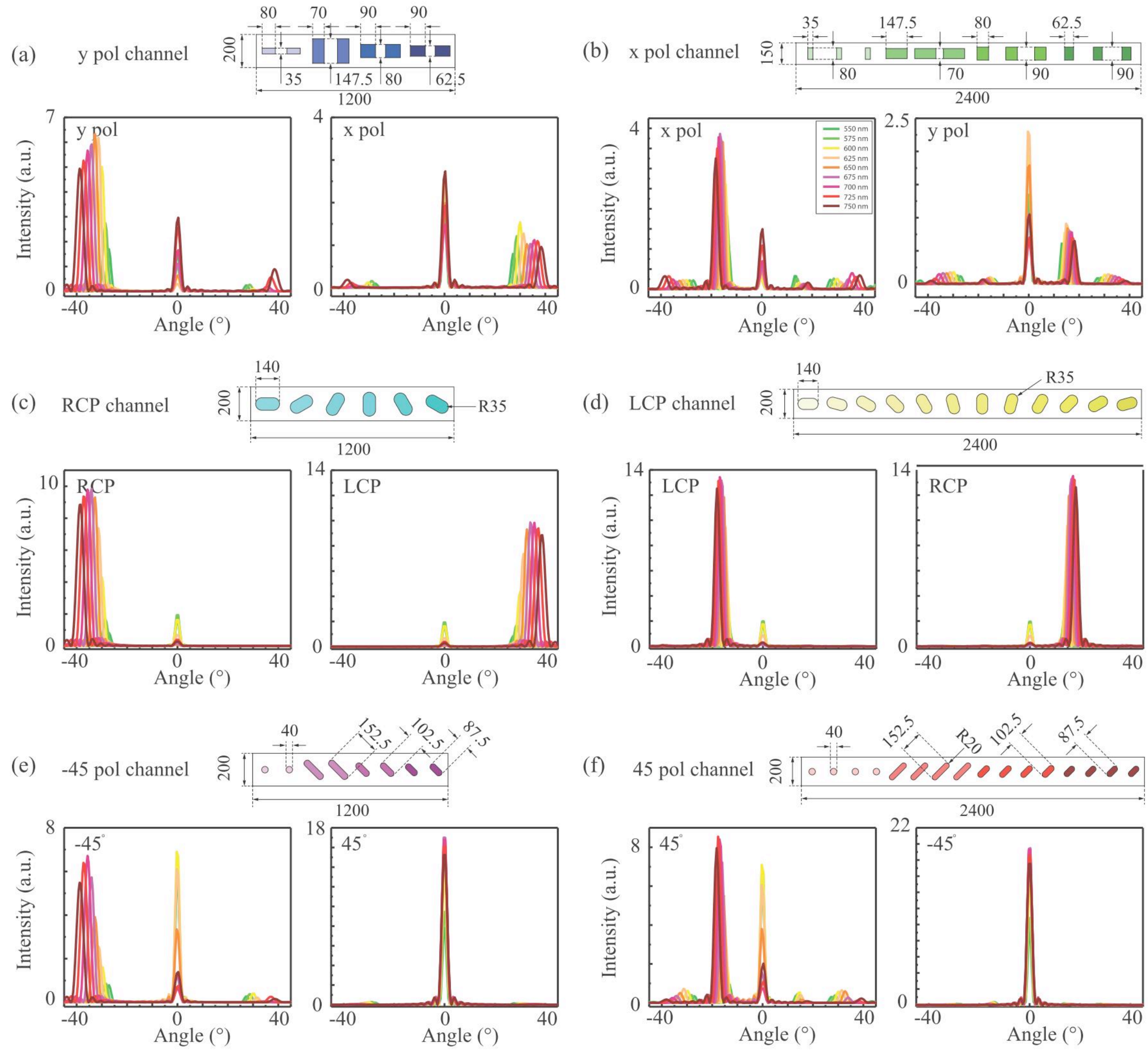

Figure S3. (a) Angular diffraction pattern for vertical (*y*-polarized) polarization state analyser when illuminated with vertically polarized light (left) and horizontally polarized light (right) for wavelengths from 525 to 725 nm in 25 nm increments. Top inset shows schematic of metasurface design. (b)-(f) As (a) but for the horizontal, right circular, left circular, -45° and 45° analysing channels. In each case the left plot shows the diffraction pattern under the co-polarized case, whilst the right panel depicts that obtained when the incident beam is orthogonally polarized.

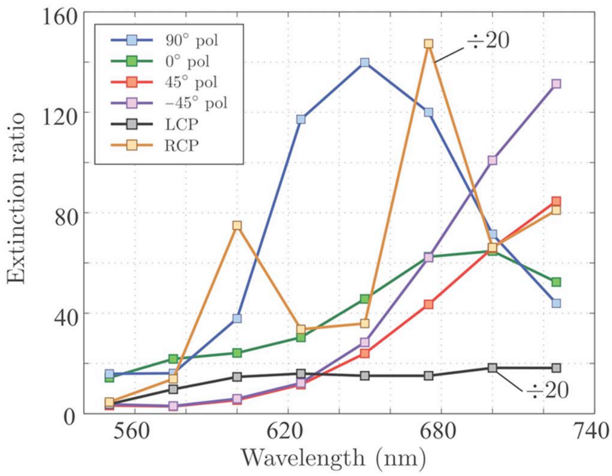

Figure S4. Extinction ratio for each detection channel. Note plots for LCP and RCP channels have been scaled by a factor of 20 for ease of comparison.

Supporting Information 4 - Calibration

Light from a super continuum laser (SC-450, Fianium), combined with an acousto optic filter (AOTF-Dual from Fianium) was passed through a polarization state generator comprising a broadband wire polarizer (Edmund Optics) and an optional achromatic quarter waveplate (AQWP05M-600, Thorlabs). Our calibration procedure follows that proposed by Azzam and Lopez [3], whereby we first use a linear polarizer in the illumination path, which is rotated from 0° to 360°, in 10° increments. An image is obtained using a sCMOS camera (Edge 5.5, PCO) for each orientation. Simultaneously the reference intensity is read using the power meter (Maestro, Gentec-EO). Subsequently the quarter waveplate is inserted after the linear polarizer with its fast axis at $+45^{\circ}$ with respect to the transmission axis of the polarizer to produce RCP light. The camera image and power meter reading are again recorded. Finally, the quarter waveplate is turned to -45° so as to generate LCP light and a last set of readings are recorded. The transverse locations of the six diffraction spots arising from each metasurface for a single wavelength were determined from a suitably chosen image and the integrated intensity within a measurement window centered on the peak locations were found, thereby emulating six detectors. The size of the integration window did not prove to be critical during these experiments as long as the intensity of the diffraction peak was small at the periphery of the window. Integrated intensity readings were then normalized by the reference intensity reading from the power meter. For the linearly polarized incident states, measured intensities for different polarizer orientations were averaged pairwise e.g $I_{0^\circ} = \left(I_{0^\circ} + I_{180^\circ}\right)/2$; $I_{10^\circ} = \left(I_{10^\circ} + I_{190^\circ}\right)/2$, ..., so as to remove errors due to a possible tilt misalignment of the polarizer. Readings for circularly polarized input light were processed in the same manner but without averaging. Once all intensity data was obtained, all readings were renormalised to the maximum intensity value within each data set. The first three columns of the instrument matrix were then obtained from the linearly polarized incident light only, by performing a minimum least-squares harmonic fit on the intensity reading. The fourth column of the instrument matrix follows from finding half the difference of the RCP and LCP intensity readings.

Supporting Information 5 - Wavelength dependence of instrument matrix

We have performed the calibration procedure described above for wavelengths ranging from 550 nm to 725 nm in equal increments of 25 nm. The resulting instrument matrices are found to be:

$$A_{550} = \begin{pmatrix} 0.2536 & 0.1563 & 0.0010 & 0.0018 \\ 0.2184 & -0.1467 & 0.0025 & -0.0060 \\ 0.5460 & -0.0135 & 0.0719 & -0.4403 \\ 0.3439 & -0.0044 & -0.0178 & 0.2382 \\ 0.1759 & -0.0070 & 0.0727 & -0.0062 \\ 0.1308 & -0.0071 & -0.0304 & 0.0051 \end{pmatrix}, A_{575} = \begin{pmatrix} 0.2094 & 0.1352 & 0.0007 & -0.0004 \\ 0.2014 & -0.1434 & 0.0063 & -0.0028 \\ 0.5362 & -0.0178 & 0.0665 & -0.4538 \\ 0.3310 & 0.0039 & -0.0213 & 0.2357 \\ 0.2167 & 0.0031 & 0.1272 & -0.0069 \\ 0.1296 & 0.0003 & -0.0449 & 0.0017 \end{pmatrix},$$

$$A_{600} = \begin{pmatrix} 0.1865 & 0.1419 & -0.0015 & 0.0010 \\ 0.2380 & -0.2044 & 0.0046 & -0.0011 \\ 0.5258 & -0.0203 & 0.0645 & -0.4637 \\ 0.4432 & 0.0174 & -0.0386 & 0.3650 \\ 0.2548 & 0.0181 & 0.1832 & -0.0022 \\ 0.1624 & 0.0149 & -0.0999 & 0.0082 \end{pmatrix}, A_{625} = \begin{pmatrix} 0.2018 & 0.1627 & 0.0000 & 0.0028 \\ 0.2339 & -0.2033 & -0.0001 & -0.0019 \\ 0.3746 & -0.0004 & 0.0443 & -0.3513 \\ 0.5228 & 0.0241 & -0.0507 & 0.4795 \\ 0.1807 & 0.0067 & 0.1302 & 0.0048 \\ 0.2454 & 0.0228 & -0.1858 & 0.0182 \end{pmatrix},$$

$$A_{650} = \begin{pmatrix} 0.2754 & 0.2287 & 0.0069 & -0.0078 \\ 0.2447 & -0.2033 & 0.0001 & -0.0063 \\ 0.4750 & 0.0037 & 0.0582 & -0.4584 \\ 0.4484 & 0.0183 & -0.0416 & 0.3928 \\ 0.2210 & -0.0005 & 0.1709 & 0.0059 \\ 0.2747 & 0.0110 & -0.2224 & 0.0245 \end{pmatrix}, A_{675} = \begin{pmatrix} 0.2557 & 0.2116 & 0.0024 & -0.0104 \\ 0.1350 & -0.1013 & 0.0061 & -0.0066 \\ 0.4865 & 0.0044 & 0.0561 & -0.4690 \\ 0.2285 & 0.0110 & -0.0178 & 0.1860 \\ 0.1991 & -0.0021 & 0.1610 & -0.0033 \\ 0.1375 & -0.0014 & -0.1077 & 0.0058 \end{pmatrix},$$

$$A_{700} = \begin{pmatrix} 0.2843 & 0.1562 & -0.0019 & -0.0093 \\ 0.1505 & -0.0470 & 0.0104 & -0.0063 \\ 0.5593 & -0.0006 & 0.0621 & -0.4203 \\ 0.2463 & 0.0039 & -0.0101 & 0.1279 \\ 0.2976 & -0.0018 & 0.1844 & -0.0074 \\ 0.1759 & -0.0041 & -0.0662 & 0.0055 \end{pmatrix}, A_{725} = \begin{pmatrix} 0.4494 & 0.1121 & 0.0009 & 0.0081 \\ 0.2749 & -0.0500 & 0.0100 & -0.0020 \\ 0.6431 & -0.0002 & 0.0456 & -0.2797 \\ 0.4013 & 0.0106 & -0.0043 & 0.1384 \\ 0.4572 & 0.0072 & 0.1605 & 0.0012 \\ 0.3521 & 0.0011 & -0.0832 & 0.0077 \end{pmatrix}$$

Supporting Information 6 - Information capacity

To calculate the information capacity we follow the method described in [4]. Specifically, we adopt a Gaussian noise model for each individual detection channel. The noise variance for each channel was derived from the residuals found after fitting of the experimental intensity data (see Calibration section above). With this noise model in hand, the Fisher information **J** for estimation of the Stokes vector **S** was derived as detailed in Ref. [4]. Treating estimation of S_0 as a marginal parameter, the reduced Fisher information matrix $\mathbf{J}'$ was found, so as to consider the precision in estimation of the state of polarization. An ellipsoidal volume of uncertainty in the normalised Poincaré space was then calculated as defined by $V = 4\pi\sqrt{c^3 / |\mathbf{J}'|}$ where c dictates the fraction of the estimates resulting from repeated experiments which lie within the ellipsoidal volume. For the normally distributed noise model used here, the probability that an estimate lies within this volume is found by considering the χ^2 cumulative distribution function at c^2. We select c = 6.25139 such that the associated probability is 0.9. Given the volume of uncertainty for polarization reconstruction, the volume of the Poincaré sphere is divided into $N = 4\pi/(3V)$ distinguishable polarization states. The information capacity then follows from [5] as $H = \log_2 N$.

Supporting Information 7 - Spectropolarimetric measurement

The liquid crystal tunable full waveplate (Thorlabs LCC1223-A) was inserted into the optical path between the IPM and the thin glass plate, as described above in the Calibration section, and was illuminated initially by linearly polarized light along the 0°, 45°, 90°, 135° and 270° directions and subsequently by LHC and RHC polarized light at λ = 650 nm. For each incident polarization the camera image was recorded. Images were subsequently processed and preliminary Müller matrices recovered using Equation 2 of the main text. The waveplate was then tuned by changing the applied voltage from 0 V to 3 V in 0.2 V steps. The Müller matrix was recovered for each voltage setting. Recovered Müller matrices were then used as initial values in the constrained maximum likelihood estimation algorithm detailed in [6] to obtain a physically admissible Müller matrix.

References:

1. N. F. Yu, P. Genevet, M. A. Kats, F. Aieta, J. P. Tetienne, F. Capasso, and Z. Gaburro, "Light Propagation with Phase Discontinuities: Generalized Laws of Reflection and Refraction," Science **334**, 333-337 (2011).
2. P. B. Johnson, and R. W. Christy, "Optical Constants of the Noble Metals," Phys. Rev. B **6**, 4370-4379 (1972).
3. R. M. A. Azzam, and A. G. Lopez, "Accurate calibration of the four-detector photopolarimeter with imperfect polarizing optical elements," J. Opt. Soc. Am. A **6**, 1513-1521 (1989).
4. M. R. Foreman, and P. Török, "Information and resolution in electromagnetic optical systems," Phys. Rev. A **82**, 043835 (2010).
5. C. E. Shannon, "A mathematical theory of communication," SIGMOBILE Mob. Comput. Commun. Rev. **5**, 3-55 (2001).
6. A. Aiello, G. Puentes, D. Voigt, and J. P. Woerdman, "Maximum-likelihood estimation of Mueller matrices," Opt. Lett. **31**, 817-819 (2006).